GA–A26657

FULLY ELECTROMAGNETIC GYROKINETIC EIGENMODE ANALYSIS OF HIGH-BETA SHAPED PLASMAS

by
E.A. BELLI and J. CANDY

MAY 2010

GENERAL ATOMICS

DISCLAIMER

GA–A26657

FULLY ELECTROMAGNETIC GYROKINETIC EIGENMODE ANALYSIS OF HIGH-BETA SHAPED PLASMAS

by
E.A. BELLI and J. CANDY

This is a preprint of a paper to be to be submitted for publication in Physics of Plasmas.

Work supported in part by
the U.S. Department of Energy
under DE-FG02-95ER54309

GENERAL ATOMICS ATOMICS PROJECT 03726
MAY 2010

Abstract

A new, more efficient method to compute unstable linear gyrokinetic eigenvalues and eigenvectors has been developed for drift-wave analysis of plasmas with arbitrary flux surface shape, including both transverse and compressional magnetic perturbations. In high-beta, strongly shaped plasmas like in the National Spherical Torus Experiment (NSTX) [M. Ono *et al.*, Nucl. Fusion **40**, 557 (2000)] , numerous branches of closely-spaced unstable eigenmodes exist. These modes are difficult and time-consuming to adequately resolve with existing linear initial-value solvers, which are further limited to the most unstable eigenmode. The new method is based on an eigenvalue approach and is an extension of the GYRO code [J. Candy and R.E. Waltz, J. Comput. Phys. **186**, 545 (2003)], reusing the existing discretization schemes in both real and velocity space. Unlike recent methods, which use an iterative solver to compute eigenvalues of the relatively large gyrokinetic response matrix, the present scheme computes the zeros of the much smaller dielectric matrix using a direct method. In the present work, the new eigensolver is applied to gyrokinetic stability analysis of a high-beta, NSTX-like plasma. We illustrate the smooth transformation from ion-temperature-gradient (ITG)-like to kinetic-ballooning (KBM)-like modes, and the formation of hybrid ITG/KBM modes, and further demonstrate the existence of high-k Alfvénic drift-wave "cascades" for which the most unstable mode is a higher excited state along the field line. A new compressional electron drift wave, which is driven by a combination of strong beta and pressure gradient, is also identified for the first time. Overall, we find that accurate calculation of stability boundaries and growth rates cannot in general ignore the compressional component, $\delta B_{\parallel}$, of the perturbation.

I. INTRODUCTION

The goal of this paper is to develop an understanding of linear high-n drift waves in high-beta plasmas with strong cross-sectional shaping. The approach is *exact* within the context of standard gyrokinetic theory [1–3], without approximations (for example, bounce-averaged electrons, long wavelength, reduction from integro-differential to differential equations, etc) usually applied for analytical tractibility or numerical simplicity.

In high-beta, strongly shaped plasmas like in the National Spherical Torus Experiment (NSTX) [4], numerous branches of closely-spaced unstable eigenmodes exist. In our experience, when modes are closely spaced, it is difficult and time-consuming to resolve the most unstable mode using the linear initial-value approach. To overcome these and other difficulties encountered in simulating NSTX plasmas, we have developed a new, more efficient method to compute unstable linear eigenvalues and eigenvectors. The method is valid for tokamak plasmas with arbitrary shape, and can retain both the compressional and transverse components of the magnetic perturbation. The new method is a simple extension of the GYRO code [5], and reuses the existing discretization schemes in both real and velocity space. Existing methods for solving the linear gyrokinetic eigenvalue problem fall into two general categories: *gyrokinetic eigenvalue solvers*, which use an iterative approach to compute eigenvalues of the relatively large gyrokinetic response matrix [6, 7], and *field dispersion-relation solvers*, which compute the zeros of the much smaller dielectric matrix using a direct method. The former solvers are too expensive for routine linear analysis and are not discussed further. On the other hand, there are numerous examples in the literature of the latter method, the earliest and still one of the most capable being due to Rewoldt [8]. Certain solvers distinguish themselves with a particular capability: for example, global capability [9] or the ability to compute stable eigenmodes [10]. The present solver is unique in that all the linear physics capabilities of GYRO can be retained, including pitch-angle collisions (although at significantly increased computational expense), global effects (since the ballooning transform is not used), finite plasma rotation, general plasma shape and full electromagnetic perturbations. The solver is parallelized, with all costly matrix operations (LU decomposition, inverse, matrix-matrix multiply) implemented fully in BLAS and LAPACK. A typical collisionless electromagnetic eigenvalue and eigenvector can be computed at standard resolution in about 5 seconds on a single 2.66GHz core.

Most studies of gyrokinetic transport, even in high-beta plasmas, have retained only the transverse electromagnetic perturbations, $\delta A_\parallel$, and neglected the compressional magnetic perturbations, $\delta B_\parallel$. While for most experimentally-relevant gyrokinetic studies of tokamaks, the impact of including $\delta B_\parallel$ is negligible due to the low beta, these effects can be large in spherical torus machines. Before the recent addition of $\delta B_\parallel$ to GYRO, GS2 [11, 12] was the only nonlinear gyrokinetic code to include the compressional response. For this reason, gyrokinetic studies of transport in high-beta plasmas including $\delta B_\parallel$ have been done almost exclusively with GS2. In early linear simulations with GS2, Kotschenreuther *et al.* [13] showed that neglecting $\delta B_\parallel$ in high-beta plasmas can lead to a significant underestimate of the ion-temperature-gradient (ITG) growth rate, as finite $\delta B_\parallel$ counteracts the stabilizing influence of the pressure-induced diamagnetic well [14]. Subsequently, studies of the effects of $\delta B_\parallel$ have focused primarily on experimental modeling of spherical tokamak plasmas. In NSTX plasmas, the role of the large trapped electron fraction in stabilization of the kinetic ballooning mode (KBM) has been examined [15], and the stabilizing influence of $\delta B_\parallel$ on electron-temperature-gradient (ETG) modes has also been reported [16]. It was similarly reported for high-mode (H-mode) plasmas in the Mega-Ampère Spherical Tokamak (MAST) [17] that the stabilization of ETG modes is sensitive to the inclusion of $\delta B_\parallel$ [18]. In contrast, studies of MAST plasmas also found that $\delta B_\parallel$ is not important for a description of the micro-tearing instability [19].

In the present work, we use the new GYRO eigensolver to systematically analyze the gyrokinetic stability of high-beta plasmas. The results in this paper are based on parameter scans about nominal values derived from an NSTX discharge centered at $r/a = 0.7$. In the analysis, we include full (i.e., compressional and transverse) electromagnetic perturbations and, through calculation of both dominant and sub-dominant eigenmodes, can identify regimes in which the oft-neglected compressional magnetic component of the perturbation is important.

The remaining content of this paper is organized as follows. In Sec. II, the basic simulation equations and eigensolver approach are described. In Sec. III, numerical results from linear gyrokinetic simulations of high-beta plasmas with the eigenvalue solver are presented. Finally, a brief summary is given in Sec. IV. We also give a description of the numerical implementation of the eigenvalue solver in the Appendix.

II. GYROKINETICS AT HIGH BETA IN SHAPED PLASMAS

In this section we write the equations for the full gyrokinetic-Maxwell system [1–3] including compressional waves, valid for arbitrary plasma cross-sectional shape, including, for example, up-down asymmetry. To make the beta-dependence of the equilibrium clear, we also make connection to the Grad-Shafranov equation. The system of integro-differential equations is then solved, without approximation, to obtain the linear Maxwell dispersion relation.

A. Local plasma equilibrium

In what follows we briefly summarize the *local geometry method* [20] suitable for both neoclassical and gyrokinetic analysis in the case of general flux-surface shape. First, one writes the magnetic field in Clebsch form [21] using nonorthogonal field-aligned coordinates (ψ, θ, α):

$$\mathbf{B} = \nabla\alpha \times \nabla\psi \quad \text{such that} \quad \mathbf{B}\cdot\nabla\alpha = \mathbf{B}\cdot\nabla\psi = 0\ . \tag{1}$$

The angle α is written in terms of the toroidal angle φ as $\alpha \doteq \varphi + \nu(\psi,\theta)$. In Eq. (1), ψ is poloidal flux divided by 2π, and θ simultaneously refers to an angle in the poloidal plane (at fixed φ) and a parameterization of distance along a field line (at fixed α). In these coordinates, the Jacobian is

$$\mathcal{J}_\psi \doteq \frac{1}{\nabla\psi\times\nabla\theta\cdot\nabla\alpha} = \frac{1}{\nabla\psi\times\nabla\theta\cdot\nabla\varphi}\ . \tag{2}$$

By writing $\mathbf{B}$ in standard form

$$\mathbf{B} = \nabla\varphi\times\nabla\psi + I(\psi)\nabla\varphi\ , \tag{3}$$

we can relate ν to the current function, I, according to

$$\nu(\psi,\theta) = -I(\psi)\int_0^\theta \mathcal{J}_\psi\,|\nabla\varphi|^2\,d\theta\ . \tag{4}$$

Next, we introduce the *effective magnetic field strength*, $B_{\rm unit}$ [20, 22], defined with reference to a global equilibrium through the relation

$$\frac{\partial\psi}{\partial r} = \frac{r}{q}B_{\rm unit}\ . \tag{5}$$

It is important to note that $B_{\rm unit}$, unlike B, is constant on a flux surface. In Eq. (5), r is the effective minor radius of the flux surface, which is defined for arbitrary plasma shape in Ref. [20].

B. Isolation of the MHD pressure-gradient effect

In analyses based on model s-α geometry, it is customary to compute stability boundaries as a function of the so-called *MHD-α parameter* (see, for example, Ref. [15])

$$\alpha_p = -q^2 R_0 \frac{8\pi}{B_0^2}\frac{dp}{dr} \, , \tag{6}$$

where R_0 and B_0 are the on-axis major radius and magnetic field, respectively, and $p = \sum_a n_a T_a$ is the total plasma pressure. Keeping in mind that generalizations of α_p to general geometry are not unique, we define a *generalized MHD-α parameter*

$$\alpha_{p,\rm unit} = -q^2 R_0 \frac{8\pi}{B_{\rm unit}^2}\frac{dp}{dr} \, , \tag{7}$$

where R_0 is the effective major radius defined in Ref. [20]. To effectively adjust $\alpha_{p,\rm unit}$ without modifying the background gradients (i.e., without modifying the diamagnetic frequency in the gyrokinetic equation) we introduce an artificial scaling parameter

$$c_{p'} \doteq \text{geometric pressure-gradient scaling parameter} \, . \tag{8}$$

In the sections that follow we will show explicitly how this parameter appears in the Grad-Shafranov equation and in the the drift velocity. In terms of $c_{p'}$, the effective MHD-α parameter is

$$\alpha_{p,\rm unit} \rightarrow -q^2 R_0 \frac{8\pi}{B_{\rm unit}^2}\frac{dp}{dr}\, c_{p'} \, . \tag{9}$$

C. The Grad-Shafranov equation

The flux-surface shape is determined by the Grad-Shafranov equation

$$R^2 \nabla \cdot \left(\frac{\nabla \psi}{R^2} \right) = -c_{p'} 4\pi R^2 \frac{\partial p}{\partial \psi} - I \frac{\partial I}{\partial \psi} \, , \tag{10}$$

where I is the current function which appears in Eq. (3). To the Grad-Shafranov equation we have added the artificial coefficient $c_{p'}$ which can be adjusted to measure the effect of

plasma pressure gradient on the equilibrium *without* changing the plasma temperature or density gradient (inconsistent at fixed beta). This is explained in more detail in the next sections. The local equilibrium method [22, 23] as described in Ref. [20] and employed here, ensures that for any choice of local equilibrium parameters (such as safety factor q, plasma elongation κ, aspect ratio R/a, and so on) the gyrokinetic equations see a true Grad-Shafranov equilibrium.

D. The electromagnetic gyrokinetic equation

The linear gyrokinetic equation [1–3] may be written as

$$\frac{\partial h_a}{\partial t} + \left(v_\parallel \mathbf{b} + \mathbf{v}_d\right) \cdot \nabla H_a + \frac{c}{B}\, \mathbf{b} \times \nabla \Psi_a \cdot \nabla f_{0a} = C_a(H_a) \; . \tag{11}$$

where f_{0a} is the equilibrium distribution which must be a local Maxwellian

$$f_{0a} = \frac{n_a}{(2\pi T_a/m_a)^{3/2}} \exp\left(-\frac{m_a v^2}{2T_a}\right) = n_a f_{\mathrm{M}a} \; . \tag{12}$$

The function H_a is the nonadiabatic distribution

$$H_a(\mathbf{R}) = \frac{z_a e f_{a0}}{T_a}\, \Psi_a(\mathbf{R}) + h_a(\mathbf{R}) \; , \tag{13}$$

such that the field potential Ψ_a includes contributions from the electrostatic fluctuations and both transverse and compressional magnetic fluctuations [3]

$$\Psi_a(\mathbf{R}) = \mathcal{G}_{0a} \left[\delta\phi(\mathbf{R}) - \frac{v_\parallel}{c}\delta A_\parallel(\mathbf{R})\right] + \frac{v_\perp^2}{\Omega_{ca} c}\, \mathcal{G}_{1a} \delta B_\parallel(\mathbf{R}) \; , \tag{14}$$

where $\Omega_{ca} \doteq z_a e B/(m_a c)$ is the cyclotron frequency. In Eq. (14), the linear operators $\mathcal{G}_{0a}$ and $\mathcal{G}_{1a}$ arise from gyro-averaging. If we write the fields in spectral form as

$$z(\mathbf{R}) = \sum_{\mathbf{k}_\perp} e^{iS(\mathbf{R})} \bar{z}(\mathbf{k}_\perp) \; , \tag{15}$$

then these operators have the following spectral representations

$$\mathcal{G}_{0a}\, z(\mathbf{R}) = \sum_{\mathbf{k}_\perp} e^{iS(\mathbf{R})} J_0(k_\perp \rho_a) \bar{z}(\mathbf{k}_\perp) \; , \tag{16}$$

$$\mathcal{G}_{1a}\, z(\mathbf{R}) = \sum_{\mathbf{k}_\perp} e^{iS(\mathbf{R})} \frac{J_0(k_\perp \rho_a) + J_2(k_\perp \rho_a)}{2} \bar{z}(\mathbf{k}_\perp) \; , \tag{17}$$

where $\mathbf{k}_\perp = -i\nabla_\perp$, and the Larmor radius is $\rho_a \doteq v_{ta}/\Omega_{ca}$ with $v_{ta} \doteq \sqrt{T_a/m_a}$.

The drift velocity in Eq. (11) is written as

$$\mathbf{v}_d = \frac{v_\parallel^2 + v_\perp^2/2}{\Omega_{ca} B}\, \mathbf{b} \times \nabla B + c_{p'} \frac{4\pi v_\parallel^2}{\Omega_{ca} B^2} \mathbf{b} \times \nabla p \,. \tag{18}$$

Once again we have introduced the artificial parameter $c_{p'}$ to measure the geometric pressure gradient effect without having to change the background profile gradients. The effect of the pressure gradient, dp/dr, on the drift velocity is complicated in the case of general flux-surface shape. The explicit dependence is described in detail in Ref. [20]. It is important to note that it is the pressure gradient, not the pressure, that enters the gyrokinetic equation. On the other hand, the pressure itself enters the Maxwell equations when they are written in dimensionless form.

E. The gyrokinetic Maxwell equations

The corresponding gyrokinetic Maxwell equations [3] are given by

$$-\frac{1}{4\pi}\nabla_\perp^2 \delta\phi + \sum_a \frac{z_a^2 e^2}{T_a} \int d^3v\, f_{0a} \delta\phi \;= \sum_a z_a e \int d^3v\, \mathcal{G}_{0a} H_a \,, \tag{19}$$

$$-\frac{1}{4\pi}\nabla_\perp^2 \delta A_\parallel \;= \sum_a z_a e \int d^3v\, \frac{v_\parallel}{c}\, \mathcal{G}_{0a} H_a \,, \tag{20}$$

$$-\frac{1}{4\pi}\delta B_\parallel \;= \sum_a z_a e \int d^3v\, \frac{v_\perp^2}{\Omega_{ca} c}\, \mathcal{G}_{1a} H_a \,. \tag{21}$$

To elucidate the beta-dependence of these equations, we introduce the dimensionless quantities

$$\delta\hat{\phi} = \frac{e\delta\phi}{T_e}\,, \quad \delta\hat{A}_\parallel = \frac{c_s}{c}\frac{e\delta A_\parallel}{T_e}\,, \quad \delta\hat{B}_\parallel = \frac{\delta B_\parallel}{B_{\rm unit}}\,, \quad \text{and} \quad \hat{H}_a = \frac{H_a}{n_e f_{{\rm M}a}}\,, \tag{22}$$

where $c_s \doteq \sqrt{T_e/m_i}$ is the ion sound speed. Some algebra shows that the equations for the dimensionless fields take the form

$$-\lambda_D^2 \nabla_\perp^2 \delta\hat{\phi} + \sum_a z_a^2 \frac{n_a T_e}{n_e T_a} \int d^3v\, f_{Ma}\, \delta\hat{\phi} \;= \sum_a z_a \int d^3v f_{{\rm M}a} \mathcal{G}_{0a} \hat{H}_a \,, \tag{23}$$

$$-\frac{2\rho_{s,{\rm unit}}^2}{\beta_{e,{\rm unit}}} \nabla_\perp^2 \delta\hat{A}_\parallel \;= \sum_a z_a \int d^3v\, f_{{\rm M}a}\, \frac{v_\parallel}{c_s} \mathcal{G}_{0a} \hat{H}_a \,, \tag{24}$$

$$-\frac{1}{\beta_{e,{\rm unit}}} \frac{B_{\rm unit}}{B} \delta\hat{B}_\parallel \;= \sum_a \int d^3v\, f_{{\rm M}a}\, \frac{m_a v_\perp^2}{2T_e} \mathcal{G}_{1a} \hat{H}_a \,. \tag{25}$$

where $\lambda_D = [T_e/(4\pi n_e e^2)]^{1/2}$ is the Debye length, and we have introduced the *effective electron beta* and *effective ion-sound gyroradius*:

$$\beta_{e,\mathrm{unit}} \doteq \frac{8\pi n_e T_e}{B_{\mathrm{unit}}^2} \quad \text{and} \quad \rho_{s,\mathrm{unit}} \doteq \frac{c_s}{eB_{\mathrm{unit}}/m_i c} \,. \tag{26}$$

In what follows, we will write the effective ion-sound gyroradius as ρ_s instead of $\rho_{s,\mathrm{unit}}$ for brevity. Note that ρ_s, unlike ρ_a, is constant on a flux surface.

F. Expansion in toroidal eigenmodes

To proceed, we expand fluctuating quantities in Fourier series, for example

$$\Psi_a = \sum_n e^{-in\alpha} \Psi_{a,n} \,. \tag{27}$$

We remark that because of the symmetry properties of the equations, it is natural to label toroidal eigenmodes with $k_\theta \rho_s$ rather than n, where $k_\theta \doteq nq/r$. For a single toroidal harmonic, the gyrokinetic equation is written symbolically as

$$\frac{\partial h_{a,n}}{\partial t} - i(\omega_\theta + \omega_d + \omega_C) H_{a,n} - i\omega_* \left(\frac{z_a e f_{0a}}{T_a} \Psi_{a,n} \right) = 0 \tag{28}$$

where ω_θ, ω_d and ω_C are differential operators:

$$-i\omega_\theta = v_\parallel (\mathbf{b} \cdot \nabla\theta) \frac{\partial}{\partial \theta} \,, \tag{29}$$

$$-i\omega_d = -in(\mathbf{v}_d \cdot \nabla\alpha) + (\mathbf{v}_d \cdot \nabla r) \frac{\partial}{\partial r} \,, \tag{30}$$

$$-i\omega_C = -i \frac{\nu_a}{2} \frac{\partial}{\partial \xi} \left(1 - \xi^2\right) \frac{\partial}{\partial \xi} \,, \tag{31}$$

$$-i\omega_* = i \frac{v_{ta}}{a} k_\theta \rho_a \left[\frac{a}{L_{na}} + \left(\frac{v^2}{2v_{ta}^2} - \frac{3}{2} \right) \frac{a}{L_{Ta}} \right] \,. \tag{32}$$

In Ref. [20] a detailed recipe for evaluation of $\mathbf{b} \cdot \nabla\theta$, $\mathbf{v}_d \cdot \nabla\alpha$ and $\mathbf{v}_d \cdot \nabla r$ for general or model flux-surface shape is given. Note that $c_{p'}$ allows us to change the pressure gradient in ω_d and the Grad-Shafranov equation without changing ω_*. While this essentially makes the pressure gradient and the species gradients inconsistent, for a fixed beta, when $c_{p'} \neq 1$, it allows us to isolate the geometric pressure gradient effect without affecting the relative magnitude of the electric and magnetic fluctutations (controlled by the explicit beta in the Maxwell equations) and the diamagnetic drifts. In Eq. (31) we have, for simplicity, retained

only the pitch-angle scattering contribution to the collision operator. In unpublished work we have verified that momentum-conserving corrections to this operator, which are in fact complicated to implement due to the energy coupling they introduce, are small (on the order of a percent or less for parameters typical of DIII-D). This is very different than the case for neoclassical transport, for which momentum conservation is required to maintain the ambipolarity of particle fluxes.

G. The Maxwell dispersion matrix

This section describes the formulation of the Maxwell dispersion matrix, which forms the basis for the new GYRO eigensolver. As outlined below, we ultimately consider the Laplace transform of the gyrokinetic-Maxwell equations, write the distribution function in terms of the fields using the gyrokinetic equation, and insert this into the Maxwell equations to form a matrix equation for the field vector $(\delta\Phi, \delta A_\parallel, \delta B_\parallel)$ in terms of the frequency. In the eigensolver, the eigenfrequencies are computed by solving for the zeros of the Maxwell dispersion matrix.

The Laplace transform [24] of a function $f(t)$, which we assume to be differentiable on $(0, \infty)$, is

$$\widetilde{f}(s) \doteq \mathcal{L}f = \int_0^\infty f(t)e^{-st}dt \tag{33}$$

whenever the integral exists for at least one value of s. In the present case, the integral will converge for $s > s_0$, where s_0 is the maximum linear growth rate. The inversion formula is given by the Bromwich integral

$$f(t) \doteq \mathcal{L}^{-1}\widetilde{f} = \frac{1}{2\pi i}\int_{c-i\infty}^{c+i\infty} \widetilde{f}(s)e^{st}ds \ , \quad 0 < t < \infty \ . \tag{34}$$

It will be convenient to use the variable $\omega = is$ in subsequent formulae. Now, from Eq. (28), solving for the distribution function in terms of the fields, it is then easy to show that

$$\widetilde{H}_a(\omega) = \mathcal{L}H_{a,n} = \frac{1}{\omega + \omega_\theta + \omega_d + \omega_C}\, ih_a(0) + \frac{\omega - \omega_*}{\omega + \omega_\theta + \omega_d + \omega_C}\left(\frac{z_a e f_{0a}}{T_a}\widetilde{\Psi}_a\right) \ , \tag{35}$$

where $\widetilde{\Psi}_a = \mathcal{L}\Psi_{a,n}$. Upon substitution of $\widetilde{H}_a(\omega)$ into the Laplace transform of the Maxwell equations, Eqs.(19)-(21), we are left with a system of equations for the fields of the form

$$\mathcal{M}^{\sigma\sigma'}(\omega)\Phi^{\sigma'}(\omega) = S^\sigma(\omega) \tag{36}$$

where σ and σ' are field indices which run from 1 to 3. The field matrix and source are given by

$$\mathcal{M}^{\sigma\sigma'}(\omega) = \delta_{\sigma\sigma'} L^{\sigma} - \sum_a \frac{z_a^2 e^2}{T_a} \int d^3v \, f_{0a} G^{\sigma a} \frac{\omega - \omega_*}{\omega + \omega_\theta + \omega_d + \omega_C} G^{\sigma' a} \, , \tag{37}$$

$$S^{\sigma}(\omega) = \sum_a z_a e \int d^3v \, G^{\sigma a} \frac{1}{\omega + \omega_\theta + \omega_d + \omega_C} \, i h_a(0) \, . \tag{38}$$

We have defined the additional 3-index vectors:

$$\left(\Phi^1, \Phi^2, \Phi^3\right) \doteq \left(\widetilde{\delta\phi}, \widetilde{\delta A_\parallel}, \widetilde{\delta B_\parallel}\right) \, , \tag{39}$$

$$\left(L^1, L^2, L^3\right) \doteq \left(-\frac{1}{4\pi}\nabla_\perp^2 + \sum_a \frac{z_a^2 e^2}{T_a} \int d^3v \, f_{0a}, \, \frac{1}{4\pi}\nabla_\perp^2, \, -\frac{1}{4\pi}\right) \, , \tag{40}$$

$$\left(G^{1a}, G^{2a}, G^{3a}\right) = \left(\mathcal{G}_{0a}, \, -\frac{v_\parallel}{c}\mathcal{G}_{0a}, \, \frac{v_\perp^2}{\Omega_{ca} c}\mathcal{G}_{1a}\right) \, . \tag{41}$$

In what follows, we will refer to $\mathcal{M}(\omega)$ as the *Maxwell dispersion matrix*. The roots of the equation $\det \mathcal{M}(\omega) = 0$ correspond to the normal modes of the system. When the velocity integrals are taken along the real velocity axes, the integrals used to compute $\mathcal{M}$ define a function of s analytic in region $s > 0$, which corresponds to the upper-half ω-plane. This means that unstable modes can be readily computed using the same (real) velocity discretization as in the initial-value problem. Calculation of stable normal modes, on the other hand, would require analytic continuation of $\mathcal{M}(\omega)$ into the lower half-plane, $\mathrm{Im}(s) \leq 0$, by deformation of the contour in velocity space, or perhaps by numerical analytic continuation.

The numerical implementation of the eigenvalue solver, which employs the existing GYRO spatial discretization methods, is described in detail in the Appendix. Here, we remark that the size of the final matrix problem is small, with $\mathrm{rank}(\mathcal{M}) = n_\sigma n_r n_b$, with n_σ the number of fields, n_r the number of radial gridpoints, and n_b the number of poloidal finite elements. For a basic electrostatic case, this can be as small as $\mathrm{rank}(\mathcal{M}) = 24$. The dominant cost is therefore not computing $\det \mathcal{M}(\omega)$, but rather computing the inverse P^{-1}, where P is the matrix representation of the propagator $P = \omega + \omega_\theta + \omega_d + \omega_C$.

III. NUMERICAL RESULTS

A. Numerical convergence

In what follows, we present benchmarks based on a finite-beta version of the Cyclone base case as well as studies of a representative NSTX-like plasma. In Table I, we summarize the simulation resolution parameters used in these studies, compared with the standard GYRO resolution. Because the eigenvalue solver reuses the existing GYRO discretization methods, we have good intuition regarding the baseline grid resolution requirements. For the Cyclone case, slightly higher radial resolution was needed due to the longer fieldline extension of the modes. For the NSTX-like case, significantly higher resolution along the field line was required to both eliminate unphysical spurious numerical modes which were observed at the standard GYRO resolution and to adequately resolve the complex structure of the physical modes.

B. Electromagnetic version of the Cyclone base case

Before carrying out parameter scans for an NSTX-like operating point, we first examine a familiar test case (the Cyclone base case [25]) consisting of a single deuterium ion species and gyrokinetic electrons: $r/a = 0.5$, $R_0/a = 2.7775$, $q = 1.4$, $s = 0.786$, $T_i/T_e = 1$, $a/L_{ni} = a/L_{ne} = 0.8$, $a/L_{Ti} = a/L_{Te} = 2.48$ and $\sqrt{m_i/m_e} = 60$. We use the s-α geometry model with $\alpha_p = 0$ (i.e. $c_{p'} = 0$) and neglect collisions.

1. Low-k_θ instabilities

We begin by verifying the implementation of compressional electromagnetic perturbations in GYRO through comparisons with the GS2 code [11, 12]. Figure 1 shows the variation of the GYRO and GS2 eigenfrequencies over an extended range of beta at a single wavenumber, $k_\theta \rho_s = 0.25$. At low beta, an ion-temperature-gradient (ITG) mode dominates and is stabilized as beta increases. Just below the threshold for the kinetic ballooning instability, $\beta_{e,\mathrm{unit}}^{\mathrm{crit}} \sim 1.3\%$, a trapped-electron mode (TEM) dominates. The TEM is shown to have essentially no dependence on beta. Finally, for $\beta_{e,\mathrm{unit}} > \beta_{e,\mathrm{unit}}^{\mathrm{crit}}$, the kinetic ballooning-mode (KBM) dominates and is further destabilized as beta increases. In tokamak and spheri-

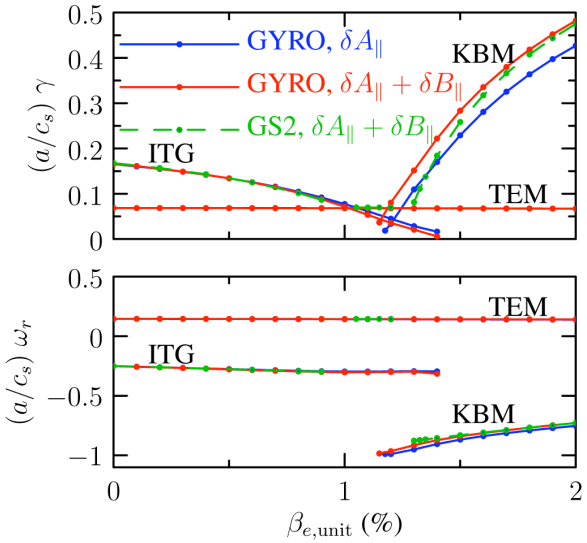

Fig. 1. Cyclone base case scan comparing GYRO (solid red) against GS2 (dashed green) results including both $\delta A_\parallel$ and $\delta B_\parallel$. The linear growth rate, γ, and real frequency, ω_r, are compared as functions of the electron $\beta_{e,\mathrm{unit}}$. Also shown are GYRO results (solid blue) for $\delta A_\parallel$ only.

cal torus plasmas, second stability can occur at high beta, depending on the value of the plasma pressure gradient, though these effects are neglected in this test case (since $c_{p'} = 0$). The overall effect of $\delta B_\parallel$ is small in this test case, except at high beta, where it is strongly destabilizing to the KBM. GYRO and GS2 have been previously benchmarked for linear and nonlinear electrostatic cases and for linear electromagnetic cases including only $\delta A_\parallel$. Figure 1 shows good intercode agreement can also be achieved at finite $\delta B_\parallel$, although we emphasize that relatively high radial and energy-grid resolution in both codes was required to achieve close agreement. We note that the slight deviation in the growth rate of the KBM near $\beta_{e,\mathrm{unit}}^{\mathrm{crit}}$ occurs even for linear electromagnetic cases including only $\delta A_\parallel$. In this region, accurate resolution of the ion drift resonance becomes important. An apparent similar deviation was also observed in a benchmark between GS2 and the GENE code, for which, similar to the GYRO results, a slightly larger KBM growth rate is predicted near threshold [26].

2. Transition to high-k_θ instabilities

In Figs. 2 and 3, we explore the transition from low-k_θ ITG/TEM/KBM modes to a high-k_θ ETG mode at fixed beta. It is found that either an ITG mode (at low beta) or a KBM (at high beta) dominates the TEM for $k_\theta \rho_s < 0.5$ and all three modes are suppressed as $k_\theta \rho_s$ increases beyond 0.5. As $k_\theta \rho_s$ increases, the TEM transforms smoothly into an ETG mode with a growth-rate that increases until about $k_\theta \rho_s = 20$. Comparing the two figures, we find that the hybrid TEM/ETG mode has a negligible dependence on beta across the entire wavenumber range. It has previously been reported that such a hybrid mode can break up at low a/L_{Te}, forming distinct TEM and ETG branches [6]. This possibility was explored here by decreasing the electron temperature gradient while holding the ion temperature gradient fixed (still with $c_{p'} = 0$). The results show that both the TEM and ETG growth rates decrease with decreasing a/L_{Te}, and that both modes become stable before they break-apart into distinct modes. We also note that, as expected, the ITG mode is not significantly affected by the changing electron temperature gradient. In contrast, the high-beta KBM is destabilized by increasing a/L_{Te}, particularly at low k_θ. This is due to the fact that the KBM is driven primarily by the normalized pressure gradient (see the MHD-α parameter in Eq. (6)) and, increasing a/L_T at fixed a/L_n increases dp/dr and thus α_p [27]. This is

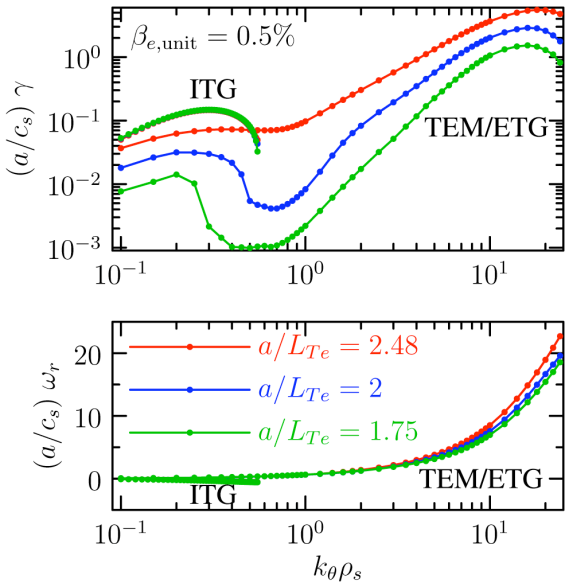

Fig. 2. Linear growth rate, γ, and real frequency, ω_r, versus $k_\theta\rho_s$ for the Cyclone base case at relatively low $\beta_{e,\mathrm{unit}}$ = 0.5%) including $\delta B_\parallel$. Three values of the electron temperature gradient are shown: a/L_{Te} = 1.75 (green curves), a/L_{Te} = 2.0 (blue curves) and a/L_{Te} = 2.48 (red curves). The hybrid TEM/ETG mode remains continuous (does not split into two separate modes) even at low a/L_{Te}.

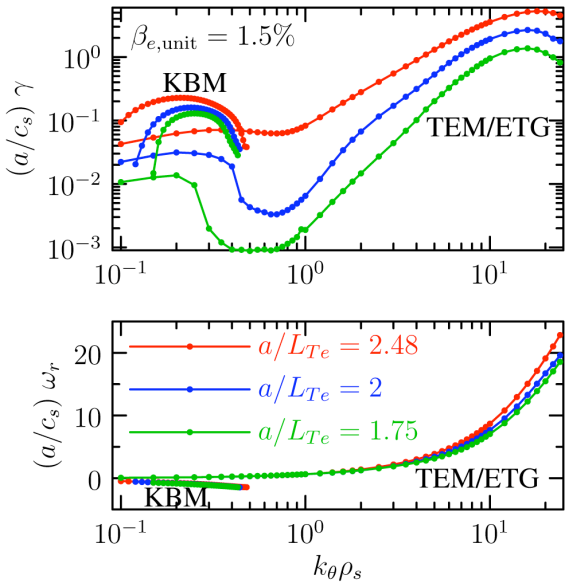

Fig. 3. Same as Fig. 2, except for somewhat higher beta ($\beta_{e,\mathrm{unit}}$ = 1.5%). Once again, the hybrid TEM/ETG mode remains continuous even at low a/L_{Te}.

analogous to Fig. 1, where α_p is increased by increasing beta.

C. Parameter scans for the high-beta NSTX-like case

We now examine the gyrokinetic linear stability with full electromagnetic physics for parameters more relevant to spherical tokamaks, including the effects of non-circular flux-surface shape and, more importantly, plasma pressure gradient. We use a model high-beta plasma based on NSTX shot #132641 at t=0.70s, which was run to explore improved confinement with strong lithium evaporation. Our model parameters are roughly based on plasma conditions at r/a=0.7. This location was chosen since there are no unstable drift-wave instabilities inside $r/a < 0.6$ due to the low shear ($|\hat{s}| < 0.1$ for $r/a < 0.55$). Still, this point is far enough from the edge where the experimental measurements may be subject to large uncertainties and the small ρ/a gyrokinetic ordering assumed in the simulation equations may fail due to steep gradients in the pedestal. For simplicity, we set the ion temperature equal to the electron temperature, and we neglect the carbon impurity species, unless specified, and thus set the ion density equal to the electron density according to quasi-neutrality. Collisions are also neglected, unless otherwise specified. Finally, we arrive at a model *NSTX-like case*: $r/a = 0.7$, $R_0/a = 1.65$, $q = 3$, $s = 0.88$, $T_e = T_D$, $a/L_{nD} = a/L_{ne} = 1$, $a/L_{TD} = a/L_{Te} = 1$ and $\beta_{e,\mathrm{unit}} = 1.7\%$. The geometric quantities are computed using the Miller local equilibrium model [20, 23] with the following shape parameters: $\partial R_0/\partial r = -0.375$, $\kappa = 2.4$, $s_\kappa \doteq (r/\kappa)\partial\kappa/\partial r = -0.12$, $\delta = 0.31$ and $s_\delta \doteq r\partial\delta/\partial r = 0.23$. For this case, the consistent value of the MHD alpha parameter is $\alpha_{p,\mathrm{unit}} = 1.0098$. Up-down symmetric flux surfaces are assumed for simplicity.

Figure 4 shows the k_θ spectrum of unstable modes for this case. Here we find surprisingly that only the low-k_θ modes are unstable; that is, no unstable modes were found beyond the range of the figure, and even the unstable modes are weakly growing. The real frequency spectrum suggests that the dominant mode seen is actually a hybrid of two ITG/KBM-like modes, which we will explore further in the sections that follow. The driving mechanisms behind the overall strong stabilization seen in Fig. 4 will also be explored in detail, focusing on the shaping effects and on the beta and plasma pressure gradient effects. For example, it is well-known that increased plasma pressure gradient can lead to a so-called Shafranov shift stabilization of drift-wave-driven instabilities by effectively increasing the good-curvature

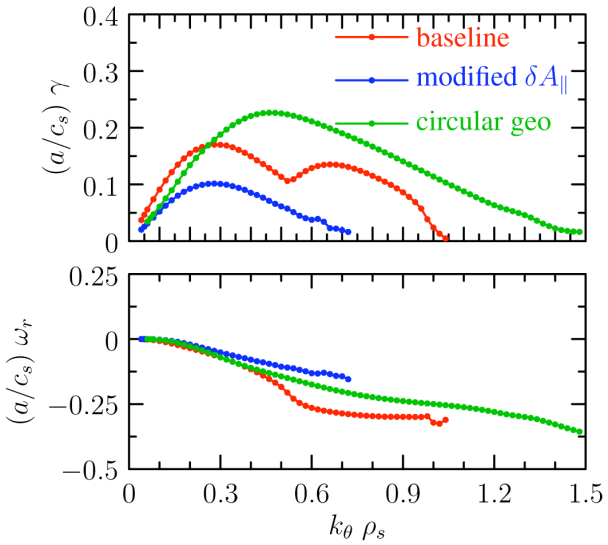

Fig. 4. Linear growth rate, γ, and real frequency, ω_r, versus $k_\theta\rho_s$ for NSTX-like parameters. GYRO simulations for the baseline case (red), which includes $\delta B_{\|}$ and shaped geometry, are compared with those which include only $\delta A_{\|}$ and are further modified by neglecting the pressure gradient in the ∇B drift, such that the curvature drift is equal to ∇B drift (blue). For the standard $\delta A_{\|}$ only case, the plasma is stable for all $k_\theta\rho_s$. Also, shown is a comparison of the baseline results with those in the circular geometry limit (green). For all three curves, no unstable modes are found at values of $k_\theta\rho_s$ beyond the range of this plot.

region of the plasma. To explore this further, below we look at scans over $c_{p'}$ and $\beta_{e,\mathrm{unit}}$ at low, intermediate, and high $k_\theta \rho_s$ to identify the type of modes, and specifically highlight the effect of the compressional magnetic perturbations via comparisons with electromagnetic results which retain $\delta A_\parallel$ but neglect $\delta B_\parallel$.

We remark that when $\delta B_\parallel$ is neglected, the plasma is stable across the entire wavenumber range for the NSTX-like case. However, MHD theory predicts that, in the $k_\theta \rightarrow 0$ limit, there is a partial cancellation between the potentially-stabilizing component of the ∇B drift proportional to the pressure gradient and the compressional magnetic field terms. Thus, neglecting $\delta B_\parallel$ can overestimate the stabilizing influence of the pressure-induced diamagnetic well. In previous numerical studies of low-k_θ ITG modes at finite-β it was observed that electromagnetic simulations which do not include $\delta B_\parallel$ – but which selectively zero the pressure gradient effect in the ∇B drift – can recover some of the destabilizing effects of $\delta B_\parallel$ [22]. Indeed, this approximation has been used in past GYRO simulations of electromagnetic turbulence [28]. Figure 4 shows that, for this case, unlike the standard $\delta A_\parallel$ only case, this modification does result in an unstable low-k_θ mode, although it is clear from the deviation from the baseline curve that not all of the dynamical effects of $\delta B_\parallel$ can be captured by this approximation. This agrees qualitatively with recent GS2 results for simple s-α plasmas [29]. Furthermore, we note that, for some high-beta DIII-D plasmas, we find this approximation to be more inaccurate than the standard $\delta A_\parallel$ only case for the entire range of $k_\theta \rho_s$. Systematic studies, either analytical or numerical, of the conditions under which this approximation is meaningful and accurate for arbitrary k_θ have not been reported. We consider such a study to be beyond the scope of this paper and do not discuss it further. Regardless, for high-beta plasmas, it is clear that inclusion of $\delta B_\parallel$ in microstability analysis is required to ensure electromagnetic effects are properly described in general.

1. Shaping effects

Figure 4 compares the eigenvalue spectrum with full shaping effects against the analogous spectrum in a circular plasma ($\kappa = 1$, $\delta = s_\kappa = s_\delta = 0$). In the latter case, only a single smooth mode exists at low k_θ, and this appears to be a continuation of the lower-k_θ shaped-plasma mode, and its growth rate is larger for $k_\theta \rho_s > 0.25$, suggesting that the shaping effects are generally stabilizing. The main shaping effects in this case appear to be the elongation,

which is known to be stabilizing, and the Shafranov shift, $\partial R_0/\partial r$, which is exerting a significant *destabilizing* effect. In fact, we found that if we eliminate the Shafranov shift in the circular case, the plasma becomes completely stable. In the end, the salient result is that the intermediate and high k_θ modes are stable and thus the shaping effects are evidently not the dominant mechanism for their stabilization.

2. Long-wavelength hybrid ITG/KBM modes

Figure 5 explores the effect of the plasma pressure gradient on low-k_θ modes, at $k_\theta \rho_s = 0.25$. In this figure, significant differences are seen when $\delta B_\parallel$ is neglected; specifically, the growth rate is largely underestimated. The overall destabilizing effect of $\delta B_\parallel$ in Fig. 5 is consistent with previous studies which showed that neglecting $\delta B_\parallel$ can lead to a large underestimation of the ITG growth rate [13]. This is a result of the fact that $\delta B_\parallel$ fluctuations ultimately counteract the stabilizing effect of the plasma diamagnetism. For both curves in Fig. 5, the mode is stabilized as the geometric pressure gradient scaling factor increases, although for the case of only transverse electromagnetic perturbations the mode is completely stabilized well below the baseline value. We have also found that purely electrostatic simulations follow a similar trend as the simulations containing only $\delta A_\parallel$ (although we do not show these results here) highlighting the strong effect of $\delta B_\parallel$ for this case.

While the real frequency spectrum indicates that these modes are ITG or KBM-like, as they are in the ion diamagnetic direction, further analysis is needed to specifically categorize them in detail. To this end, Fig. 6 shows a scan over $\beta_{e,\text{unit}}$ at various values of $c_{p'}$. Here we find that, when the geometric pressure-gradient effects are zeroed ($c_{p'} = 0$), the (blue) curve looks similar to that for the Cyclone base case in Fig. 1 in that we find a dominant ITG mode at low beta and a dominant KBM at high beta. The latter mode is dominant at the baseline values $c_{p'} = 1$ and $\beta_{e,\text{unit}} = 1.7\%$. However, unlike the Cyclone case, the ITG mode has a weak, yet destabilizing, dependence on beta. Figure 6 further shows that, as $c_{p'}$ increases, (1) the growth rate of the KBM strongly decreases, (2) the growth rate of the ITG mode weakly increases, and (3) two distinct modes merge into a hybrid ITG/KBM mode. At high $c_{p'}$, this hybrid mode is further stabilized as $c_{p'}$ increases. Figure 7 further confirms this picture by showing the structure of the eigenmodes at the baseline beta, $\beta_{e,\text{unit}} = 1.7\%$. Here, we clearly see that the dominant mode at $c_{p'}$=0 has the KBM symmetry in $\delta A_\parallel$ (out-

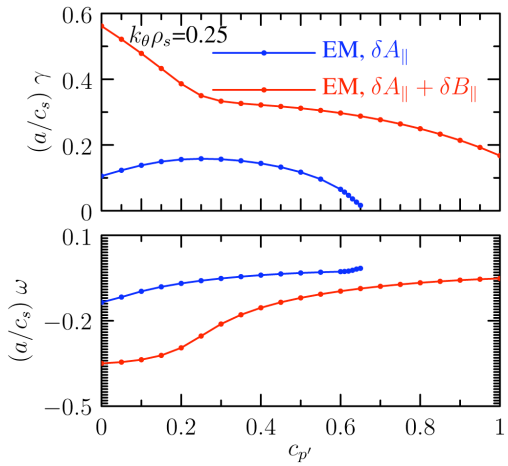

Fig. 5. Linear growth rate, γ, and real frequency, ω_r, versus the geometric pressure gradient scaling factor, $c_{p'}$. NSTX-like parameters at $k_\theta\rho_s = 0.25$ are assumed. GYRO simulations including only $\delta A_\parallel$ are compared with those including both $\delta A_\parallel$ and $\delta B_\parallel$. The unstable mode at the baseline value $c_{p'} = 1$ (note that $\alpha_{p,\mathrm{unit}} = 1.0098\ c_{p'}$) is seen only with full electromagnetic perturbations (red curve).

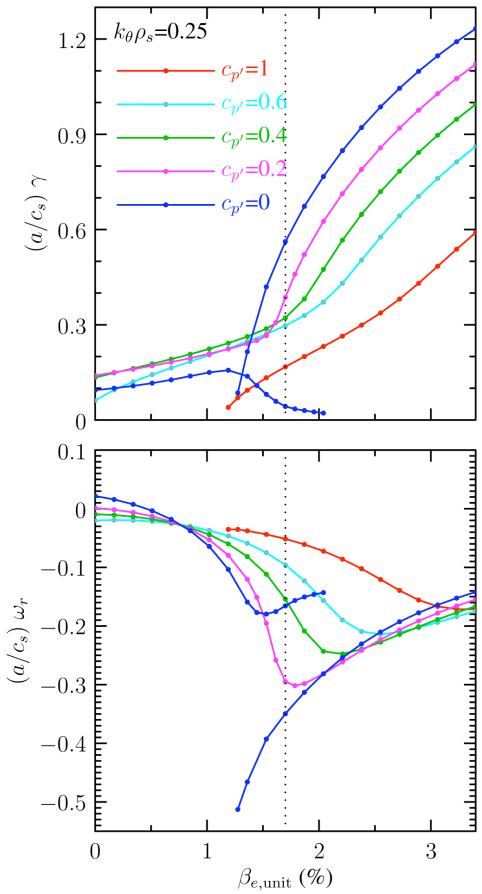

Fig. 6. Linear growth rate, γ, and real frequency, ω_r, versus electron beta, $\beta_{e,\mathrm{unit}}$, for selected values of the geometric pressure gradient scaling factor, $c_{p'}$ ($\alpha_{p,\mathrm{unit}} = 1.0098\ c_{p'}$). NSTX-like parameters at $k_\theta\rho_s = 0.25$ are assumed. These simulations include $\delta B_\parallel$. Hybrid ITG/KBM modes are seen for $c_{p'} \geq 0.2$.

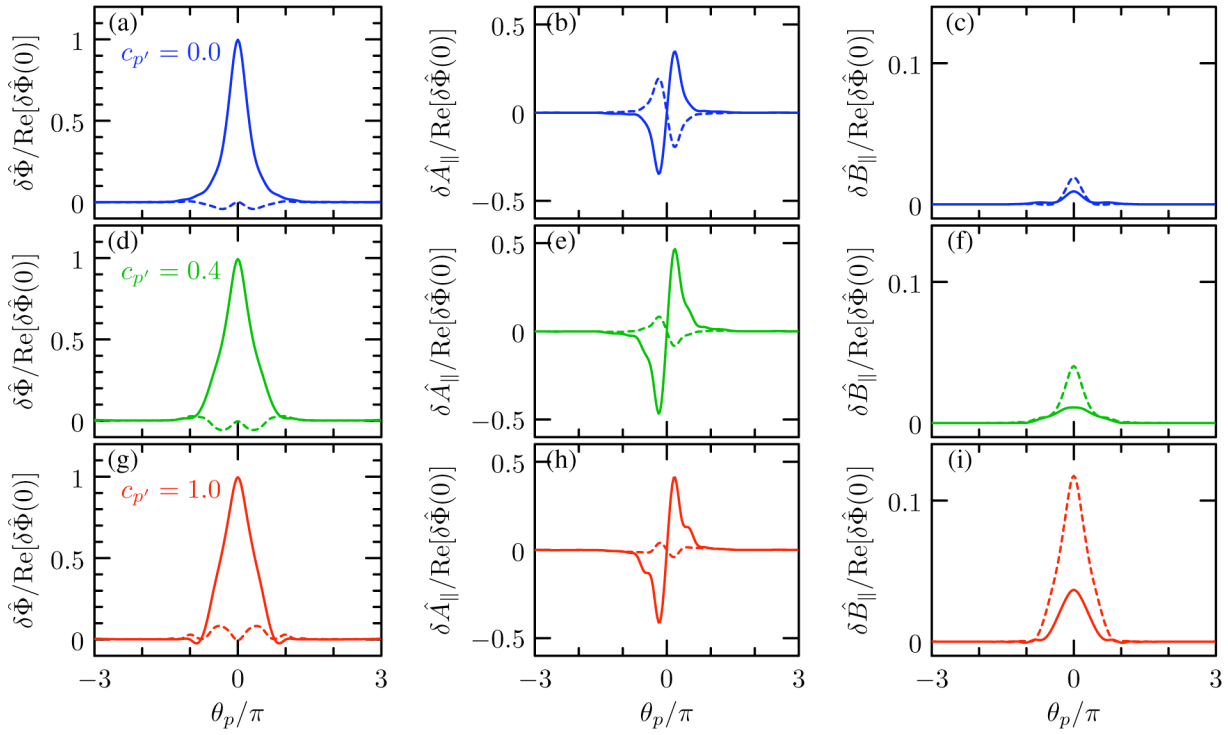

Fig. 7. Normalized field eigenfunctions plotted as a function of the ballooning angle θ_p relative to the value of the real part of the normalized electrostatic potential at θ_p=0 for the dominant mode for NSTX-like parameters at $k_\theta\rho_s$ = 0.25 including $\delta B_\parallel$. The following values of the geometric pressure gradient scaling factor are considered: $c_{p'}$ = 0 (a-c) (KBM), $c_{p'}$ = 0.4 (d-f) (hybrid ITG/KBM), $c_{p'}$ = 1 (g-i) (hybrid ITG/KBM). The solid (dashed) lines are the real (imaginary) components. Note that $\alpha_{p,\mathrm{unit}} = 1.0098\ c_{p'}$.

of-phase-symmetry of the real and imaginary components). As $c_{p'}$ increases and the hybrid mode forms, the KBM symmetry is retained. Though not shown here, we have confirmed the hybrid mode smoothly transforms from KBM to ITG symmetry as $\beta_{e,\mathrm{unit}}$ decreases, with the imaginary component of $\delta A_\parallel$ becoming smaller until it reverses to become in-phase with the real component. Figure 7 also shows that $\delta B_\parallel$ increases with $c_{p'}$, although it is still much smaller than $\delta A_\parallel$. Nevertheless, Fig. 5 shows that the compressional component still significantly influences the growth rate.

A similar picture emerges when $\delta B_\parallel$ is neglected, as shown in Fig. 8. In this case we find that the mode seen in the $\delta A_\parallel$-only case of Fig. 5 (blue curve) is actually from the ITG branch, rather than from the KBM branch as for the full electromagnetic case. Figure 8 further shows that this mode has essentially no dependence on the electron beta. However, for the hybrid ITG/KBM, similar to the case with $\delta B_\parallel$ effects, the mode is stabilized with increasing $c_{p'}$ and is completely stabilized by $c_{p'} \sim 0.65$, in accordance with Fig. 5.

3. Intermediate-wavelength hybrid ITG/KBM modes

Having identified the mode in Fig. 4 as a hybrid ITG/KBM mode, we note that there appears to be a significant transition in the mode near $k_\theta \rho_s = 0.55$. Thus, we now perform our analysis at an intermediate wavenumber of $k_\theta \rho_s = 0.6$ for comparison with the $k_\theta \rho_s$=0.25 regime. The results for the $c_{p'}$-scan are shown in Fig. 9. Two distinct modes appear for both the reduced electromagnetic ($\delta B_\parallel$ neglected) and fully electromagnetic cases. The leftmost ITG mode is eventually completely stabilized as $c_{p'}$ increases. Then a secondary mode appears which remains unstable at the baseline value only when full electromagnetic effects are retained, similar to the low-k_θ case in Fig. 5. The real frequency spectrum indicates that the second mode appears to be from the same family as the reduced electromagnetic modes. For further analysis, Fig. 10 shows a scan over $\beta_{e,\mathrm{unit}}$ at various values of $c_{p'}$, analogous to Fig. 6. For the first mode in Fig. 9, we again find distinct ITG/KBM branches ($c_{p'}$=0 and $c_{p'}$=0.15 curves in Fig. 10), with the dominant mode at the baseline beta being the KBM branch. For the secondary mode, two distinct branches are initially seen ($c_{p'} = 0.4$), but then a hybrid ITG/KBM mode forms ($c_{p'} = 0.6$) which is further stabilized with increasing $c_{p'}$ ($c_{p'} = 1$). In summary, for this case, the eigenmode plots in Fig. 11 show the KBM symmetry for the dominant mode at $c_{p'} = 0$ and the ITG symmetry for $c_{p'} = 0.4$ and the

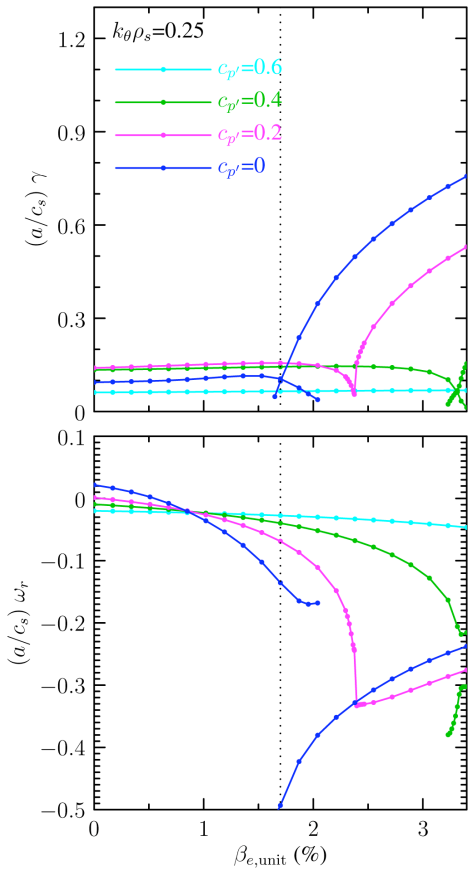

Fig. 8. Linear growth rate, γ, and real frequency, ω_r, versus the electron beta, $\beta_{e,\mathrm{unit}}$, for selected values of the geometric pressure gradient scaling factor, $c_{p'}$. NSTX-like parameters at $k_\theta\rho_s$ = 0.25 are assumed. These simulations include only $\delta A_\parallel$. In comparison with the fully electromagnetic case in figure 6, hybrid ITG/KBM modes are still seen at finite $c_{p'}$, but the unstable mode at the baseline beta has ITG rather than KBM symmtery. Note that $\alpha_{p,\mathrm{unit}} = 1.0098\, c_{p'}$.

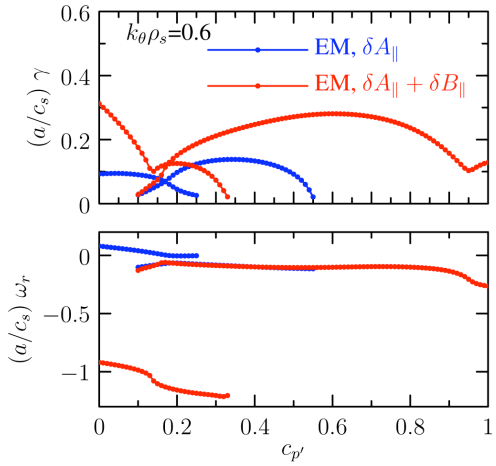

Fig. 9. Linear growth rate, γ, and real frequency, ω_r, versus the geometric pressure gradient scaling factor, $c_{p'}$. NSTX-like parameters at $k_\theta\rho_s$ = 0.6 are assumed. GYRO simulations including only $\delta A_\parallel$ are compared with those including both $\delta A_\parallel$ and $\delta B_\parallel$. The unstable mode at the baseline value $c_{p'}$ = 1 is seen only with full electromagnetic perturbations (red curve). Note that $\alpha_{p,\mathrm{unit}} = 1.0098\, c_{p'}$.

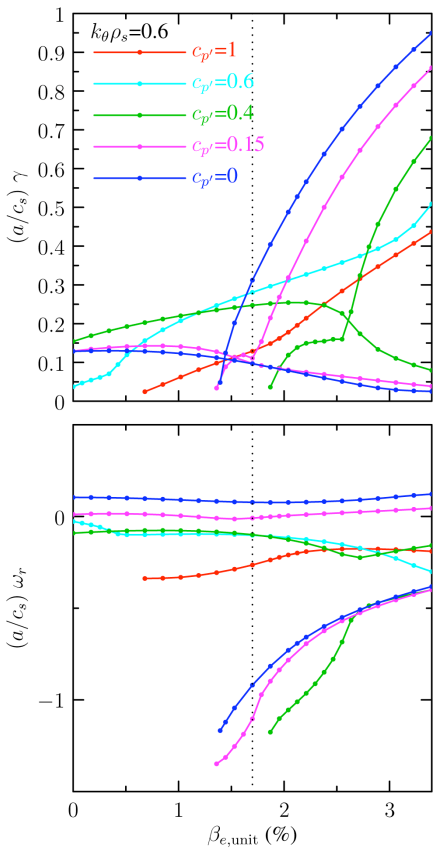

Fig. 10. Linear growth rate, γ, and real frequency, ω_r, versus the electron beta, $\beta_{e,\mathrm{unit}}$ for selected values of the geometric pressure gradient scaling factor, $c_{p'}$. NSTX-like parameters at $k_\theta\rho_s$ = 0.6 are assumed. These simulations include $\delta B_\parallel$. Hybrid ITG/KBM modes are seen at $c_{p'}$ = 0.6 and 1.0. Note that $\alpha_{p,\mathrm{unit}}$ = 1.0098 $c_{p'}$.

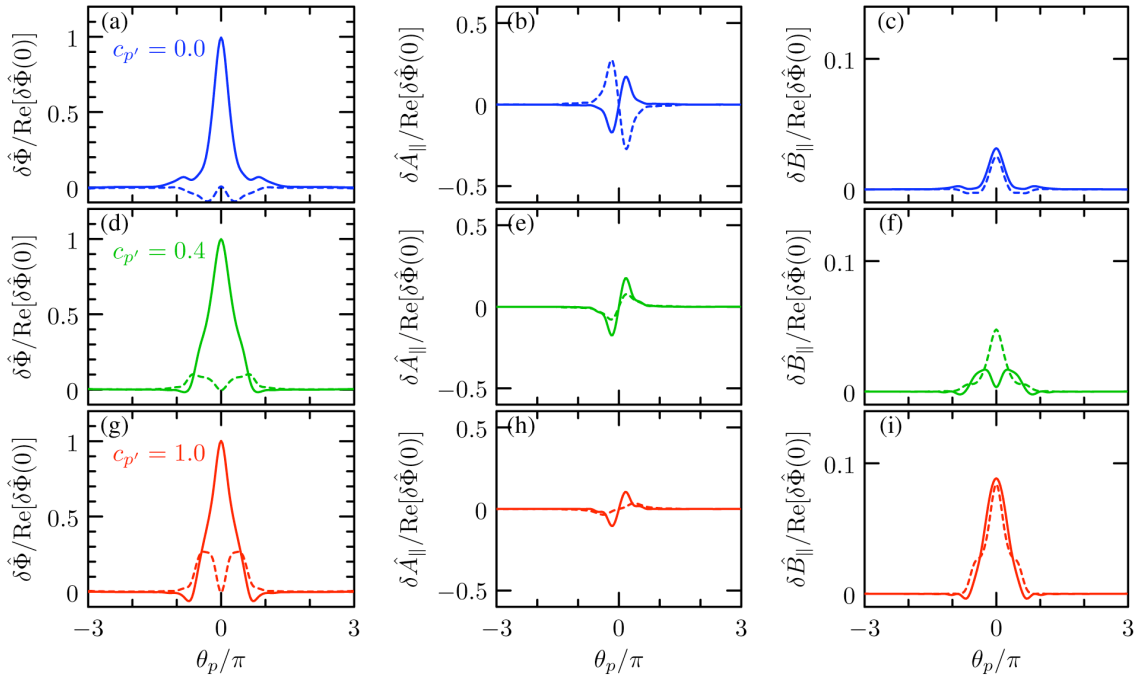

Fig. 11. Normalized field eigenfunctions plotted as a function of the ballooning angle θ_p relative to the value of the real part of the normalized electrostatic potential at θ_p=0 for the dominant mode for NSTX-like parameters at $k_\theta\rho_s$ = 0.6 including $\delta B_\parallel$. The following values of the geometric pressure gradient scaling factor are considered: $c_{p'}$ = 0 (a-c) (KBM), $c_{p'}$ = 0.4 (d-f) (ITG-like), $c_{p'}$ = 1 (g-i) (hybrid ITG/KBM). The solid (dashed) lines are the real (imaginary) components. Note that $\alpha_{p,\mathrm{unit}}$ = 1.0098 $c_{p'}$.

hybrid mode at $c_{p'} = 1$. Unlike the low-k_θ case, here we find that, at the baseline levels ($\beta_{e,\mathrm{unit}} = 1.7\%$, $c_{p'} = 1$) $\delta B_\parallel$ is as large as $\delta A_\parallel$.

Overall, relating the low- and intermediate-k_θ figures back to Fig. 4, we see that the red curve corresponds to a merger of two hybrid ITG/KBM modes, starting with KBM-like symmetry at low k_θ and transitioning to ITG-like symmetry beyond $k_\theta \rho_s = 0.5$.

4. Cascading Alfvénic drift modes

The most surprising result of Fig. 4 is the complete stabilization of modes in the high-k_θ ETG regime. This observation suggests that we analyze in detail the effects of the pressure gradient and beta at $k_\theta \rho_s = 15$. Figure 12 shows a scan over $c_{p'}$ analogous to Figs. 5 and 9. Here we find a interesting *cascade* of modes as $c_{p'}$ increases, as represented by the four peaks for the reduced electromagnetic case and the first three peaks for the fully electromagnetic case. The difference between the full and reduced electromagnetic cases for these cascading modes is less significant compared with the low-k_θ case. Furthermore, although not shown here, the cascade of modes for the electrostatic case (including only $\delta\phi$) is nearly identical to the reduced electromagnetic case and thus these modes are not strongly influenced by the Ampère equation dynamics.

The scan over $\beta_{e,\mathrm{unit}}$ in Fig. 13 for selected values of $c_{p'}$ gives us further insight. These modes appear to be *Alfvénic drift modes*, because the real frequency is on the order of the Alfvén frequency (dashed curve in Fig. 13). The cases $c_{p'} = 0$, 0.2 and 0.4 correspond to the first (leftmost) mode in Fig. 12. Unlike the low and intermediate k_θ cases, the dominant mode at $c_{p'} = 0$ is not a KBM mode, but rather a mode in the electron direction with a very weak beta dependence, similar to the TEM seen for the Cyclone base case scan in Fig. 1. The second mode in Fig. 12, represented by the $c_{p'} = 0.6$ curve in Fig. 10, has two distinct very-low-frequency branches similar to the ITG/KBM branches seen at low $c_{p'}$ for the low k_θ case. For the third mode, represented by the $c_{p'} = 0.65$ curve, only a single mode appears over this range. The eigenfunctions for these modes (see Fig. 14) shows that these cascades are actually different *excited states* along the fieldline. Specifically, the first mode is the ground state, the second mode is the first excited state, etc. In all cases, $\delta B_\parallel$ is significantly larger than $\delta A_\parallel$, in contrast with the lower-k_θ cases. Note also that with the structure of the eigenmodes becoming increasingly more complex during the cascade, very high spatial

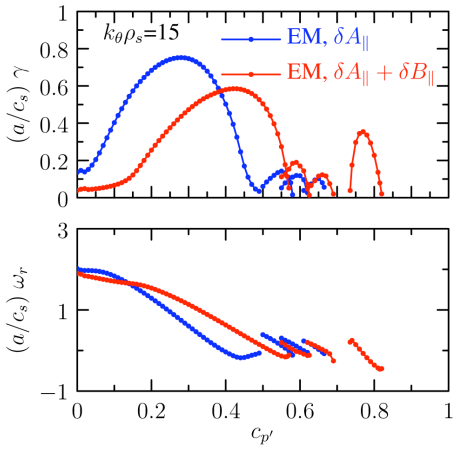

Fig. 12. Linear growth rate, γ, and real frequency, ω_r, versus the geometric pressure gradient scaling factor, $c_{p'}$. NSTX-like parameters at $k_\theta\rho_s$ = 15 are assumed. GYRO simulations including only $\delta A_\parallel$ are compared with those including both $\delta A_\parallel$ and $\delta B_\parallel$. The $\delta A_\parallel$-only modes (blue curves) and the first three fully electromagnetic modes (red curves) represent a cascade of Alfvénic modes from the ground state to excited states. A new compressional electron drift mode is seen near $c_{p'} \sim 0.75$. However, no unstable modes survive at the baseline level, $c_{p'} = 1$, such that $\alpha_{p,\mathrm{unit}} = 1.0098\, c_{p'}$.

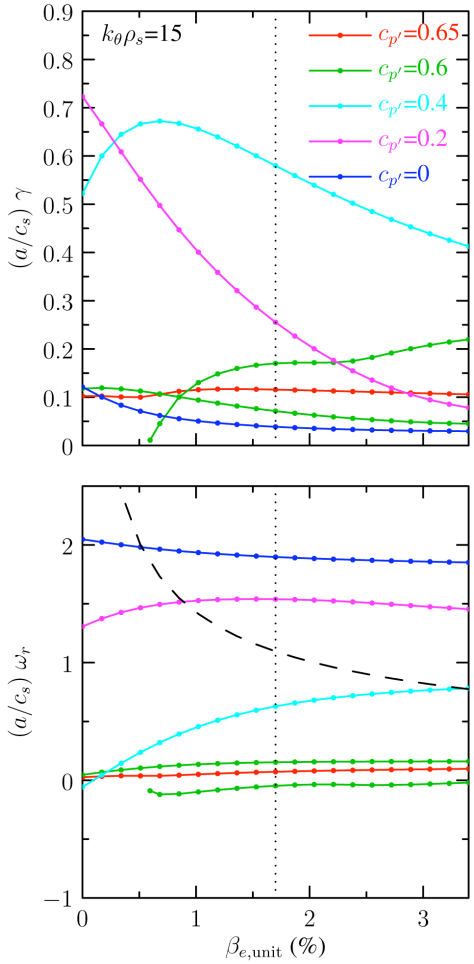

Fig. 13. Linear growth rate, γ, and real frequency, ω_r, versus the electron beta, $\beta_{e,\mathrm{unit}}$, for the cascading Alfvénic drift modes of Fig. 12 for selected values of the geometric pressure gradient scaling factor, $c_{p'}$. NSTX-like parameters at $k_\theta\rho_s$ = 15 are assumed. These simulations include $\delta B_\parallel$. $c_{p'}$ = 0.0, 0.2, and 0.4 correspond to the ground state, $c_{p'}$ = 0.6 corresponds to the first excited state, and $c_{p'}$ = 0.65 corresponds to the second excited state. The dashed line represents the Alfvén frequency. Note that $\alpha_{p,\mathrm{unit}} = 1.0098\, c_{p'}$.

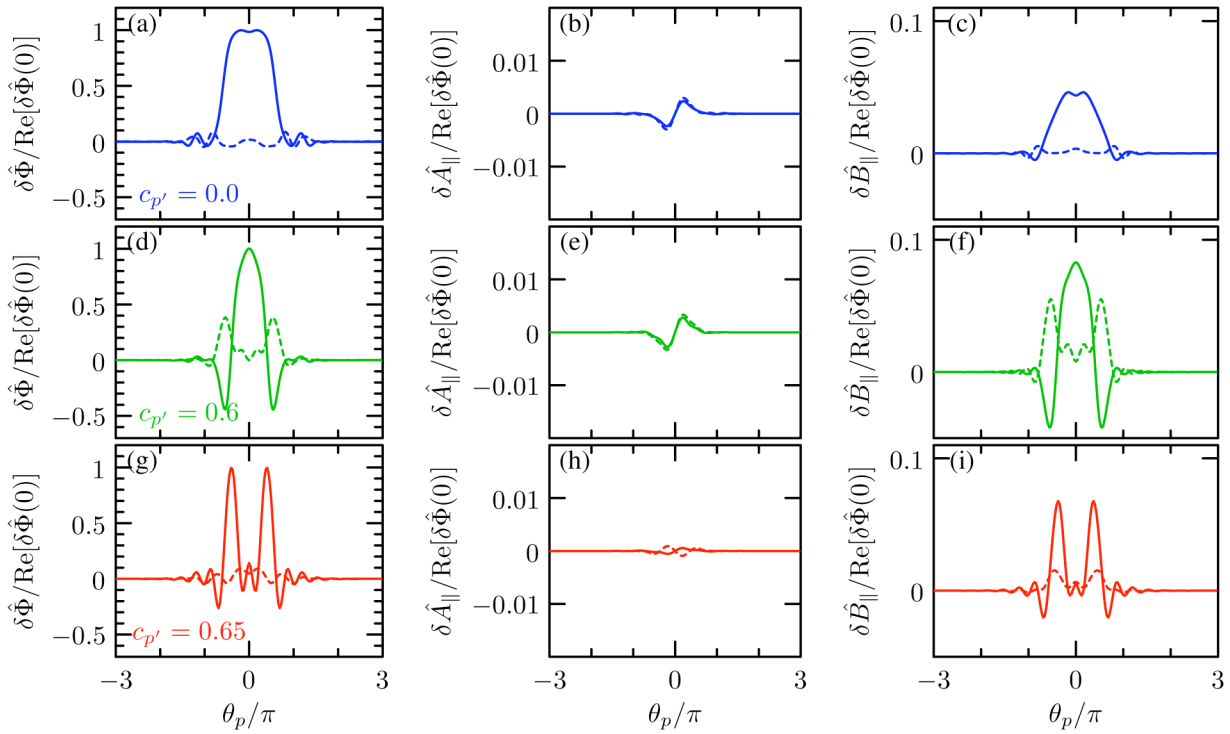

Fig. 14. Normalized Alfvénic drift eigenfunctions plotted as a function of the ballooning angle θ_p relative to the value of the real part of the normalized electrostatic potential at θ_p=0 for the dominant mode for NSTX-like parameters at $k_\theta\rho_s$=15 including $\delta B_\parallel$. The following values of the geometric pressure gradient scaling factor are considered: $c_{p'}$ = 0 (a-c) (ground state), $c_{p'}$ = 0.6 (d-f) (first excited state), $c_{p'}$ = 0.65 (g-i) (second excited state). The solid (dashed) lines are the real (imaginary) components. Note that $\alpha_{p,\mathrm{unit}} = 1.0098\, c_{p'}$.

resolution along the field lines is needed to adequately resolve them. In fact, we found that spurious computational modes can form at low resolution.

5. Compressional electron drift waves

The fourth, high-k_θ mode in Fig. 12, which appears at large $c_{p'}$ when $\delta B_\parallel$ effects are included, does not appear to be part of the initial cascade and, in fact, Fig. 15 shows that it is part of a set of *compressional electron drift waves*. This is the first time such compressional modes have been observed. For these modes, the real frequency is somewhat shifted from the Alfvén frequency and, unlike the KBM/ITG/Alfvénic drift modes, these are destabilized by simultaneous strong beta and pressure gradient. Thus, at the baseline pressure gradient, the mode is unstable only at very high beta, specifically at nearly two times the baseline value. Plots of the eigenmodes in Fig. 16 shows that these modes are in the ground state, but with very large compressional magnetic components. Although the structure is apparently simpler than for the excited-state modes, we still find that high resolution along the field lines is necessary, as otherwise the modes are essentially missed.

Overall, relating these plots back to the baseline curve in Fig. 4, at high k_θ, while the large plasma pressure gradient has stabilized the Alfvénic cascade, beta is too weak to destabilize the compressional electron drift modes, so ultimately the high k_θ-regime is stable.

6. ETG modes

In addition to the high plasma pressure gradient, these NSTX-like cases are generally difficult to simulate accurately because they reside near marginal stability. To illustrate this, Fig. 17 shows a scan over the temperature gradient scale length (equal for electrons and ions). Because we are interested in the destabilizing effects of the temperature gradient here, we take $c_{p'} = 0$ for this analysis, since increasing the temperature gradient also increases the strongly stabilizing effect of the geometric pressure gradient. Figure 17 shows most notably that the critical gradient for the high-k_θ ETG mode occurs well above the baseline level. Consistent with Fig. 12, an unstable mode does persist at the baseline level (the ground-state Alfvénic drift mode), though it is weakly growing and uncoupled from the main ETG mode. For the low-k_θ case, the KBM dominates until very low a/L_T, where the TEM

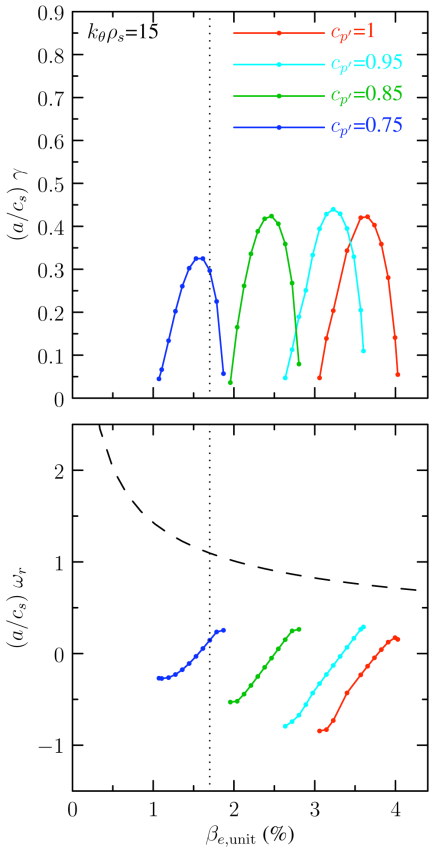

Fig. 15. Linear growth rate, γ, and real frequency, ω_r, versus the electron beta, $\beta_{e,\mathrm{unit}}$, for compressional electron drift waves ($\delta B_\parallel$ is necessary for the existence of these modes). NSTX-like parameters at $k_\theta\rho_s$ = 15 are assumed. The dashed line represents the Alfvén frequency. Note that $\alpha_{p,\mathrm{unit}}$ = 1.0098 $c_{p'}$.

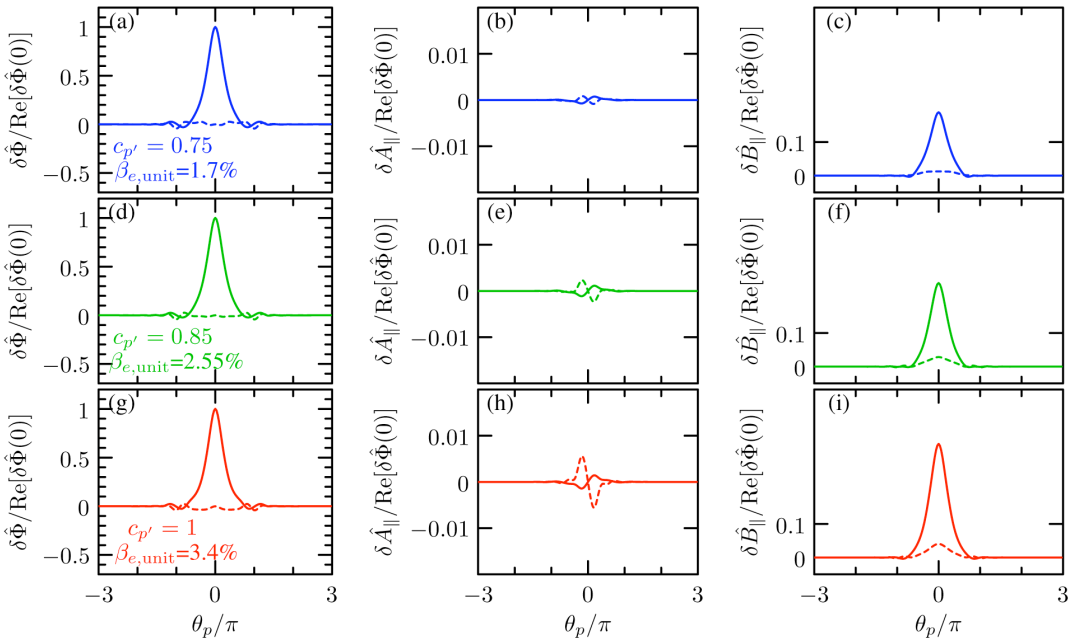

Fig. 16. Normalized compressional electron drift wave eigenfunctions plotted as a function of the ballooning angle θ_p relative to the value of the real part of the normalized electrostatic potential at θ_p=0 for the dominant mode for NSTX-like parameters at $k_\theta\rho_s$ = 15.0 including $\delta B_\parallel$. The following values of the geometric pressure gradient scaling factor and beta scaling factor are considered: $c_{p'}$ = 0.75, $\beta_{e,\mathrm{unit}}$ = 1.7% (a-c); $c_{p'}$ = 0.85, $\beta_{e,\mathrm{unit}}$ = 2.55% (d-f); $c_{p'}$ = 1, $\beta_{e,\mathrm{unit}}$ = 3.4% (g-i). The solid (dashed) lines are the real (imaginary) components. Note that $\alpha_{p,\mathrm{unit}}$ = 1.0098 $c_{p'}$.

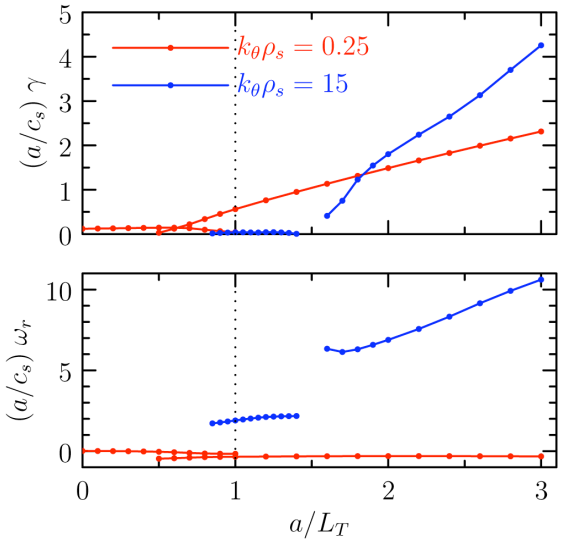

Fig. 17. Linear growth rate, γ, and real frequency, ω_r, versus temperature gradient length scale (a/L_{Ti}=a/L_{Te}). NSTX-like parameters with geometric pressure gradient scaling factor $c_{p'} = 0$ ($\alpha_{p,\mathrm{unit}} = 0$) are assumed. These simulations include $\delta B_\parallel$. The dotted line corresponds to the baseline value. Note that the critical gradient for the high-k_θ ETG mode occurs well above the baseline value.

emerges. Performing a scan over k_θ as in Fig. 4 (but at $a/L_T = 3$ rather than $a/L_T = 1$), Fig. 18 shows that the larger temperature-gradient drive is enough to destabilize the drift-mode instabilities over the entire regime, though just barely, with a weakly destabilized zone forming in the region at intermediate $k_\theta \rho_s$, and the overall spectrum appearing as a smoothly-transitioning ITG/ETG hybrid mode, similar to the hybrid TEM/ETG mode in Figs. 2 and 3. For reference, the red curve ($c_{p'} = 0$ at the baseline value of a/L_T) confirms that reducing the pressure gradient alone is not enough to drive the intermediate-k_θ modes unstable. However, once a/L_T is large enough to strongly drive the ETG mode, decreasing $c_{p'}$ further destabilizes the mode (as shown by the green curve).

7. Addition of carbon impurity and electron collision effects

Although the focus of the present work is understanding compressional electromagnetic effects rather than direct experimental comparison, we give for reference some more comprehensive simulation results. Figure 19 shows the effect of including the (large) carbon impurity fraction measured in the experiment. For these simulations, the deuterium ion parameters are modified from the pure plasma values due to quasi-neutrality and thus we have: $n_i/n_e = 0.5$, $n_c/n_e = 1/12$, $a/L_{ni} = 2.5$, $a/L_{nc} = -0.25$, $T_c = T_i$, $a/L_{Tc} = a/L_{Ti}$. The electron parameters are the same as before. Due to the significant impurity fraction in this discharge, their impact is non-negligible. However, we note that the magnitude of the growth rate for the low-k_θ mode is on the same order as the pure plasma case and the qualitative variation of the curve is retained, including, most significantly, the absence of unstable high k_θ modes. Thus, we expect our general conclusions for the pure plasma case to be relevant, though of course inclusion of the impurity dynamics is surely necessary for validation work.

In addition, due to the low temperature, electron collisions are significant. In Fig. 19 we also show the k_θ spectrum for the deuterium+carbon case, including electron collisions. The overall effect is, as expected, stabilizing for the hybrid ITG/KBM modes across the entire range. We note that, even with collisions, we do not observe any micro-tearing instabilities (dominant or sub-dominant) for this case.

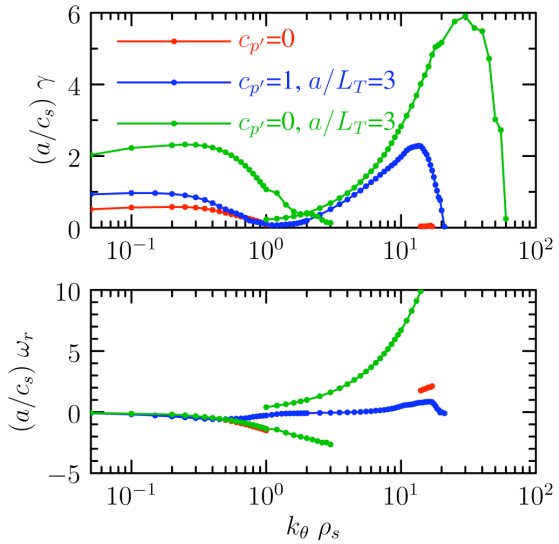

Fig. 18. Linear growth rate, γ, and real frequency, ω_r, versus $k_\theta\rho_s$ for NSTX-like parameters. GYRO simulations for the baseline temperature gradient length scale, a/L_T = 1, and geometric pressure gradient scaling factor $c_{p'}$ = 0 ($\alpha_{p,\mathrm{unit}}$ = 0) are compared with those for a/L_T = 3. These simulations include $\delta B_\parallel$. Compare with Fig. 4 with the baseline values a/L_T = 1 and $c_{p'}$ = 1, for which no unstable ETG modes were found.

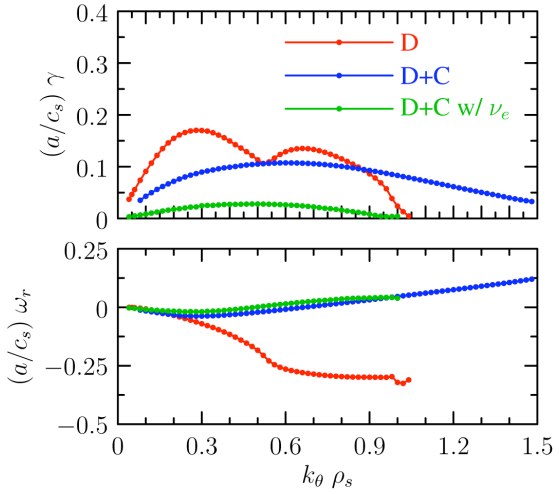

Fig. 19. Linear growth rate, γ, and real frequency, ω_r, versus $k_\theta\rho_s$ for NSTX-like parameters including $\delta B_\parallel$. GYRO simulations for the baseline (collisionless, pure-plasma) case (red curve) are compared with those for the baseline plus carbon impurities (blue curve), and the baseline plus carbon impurities and electron collisions (green curve).

IV. SUMMARY AND DISCUSSION

A new fast eigensolver in GYRO has been developed to analyze the spectrum of unstable modes in high-beta, shaped plasmas. Initial-value analysis of gyrokinetic linear stability in such plasmas is inconvenient, due to numerous, closely-spaced modes. Thus, an eigenmode analysis, which can distinguish simultaneous dominant and sub-dominant modes, is highly advantageous. Our method, which solves for the zeros of the Maxwell dispersion matrix, rather than computing the eigenvalues of the much larger dispersion matrix corresponding to the linear gyrokinetic equation, retains all of the linear physics of GYRO and is highly efficient.

Systematic studies of the effects of compressional magnetic perturbations on the linear eigenmode spectrum in high-beta plasmas were done through analysis of the dominant and sub-dominant eigenmodes in parameter scans of a representative NSTX discharge. Even for this linear analysis, these cases are found to be difficult because they are near marginal stability and are further stronglystabilized by the high plasma pressure gradient. The main results are as follows:

1. For all cases, the effects of the compressional magnetic component, $\delta B_{\parallel}$, are found to be significant, as the growth rates are largely underestimated if $\delta B_{\parallel}$ is neglected, often becoming completely stable.

2. At low and intermediate k_θ, a transition from distinct ITG and KBM modes to a hybrid ITG/KBM mode is observed at large pressure gradient.

3. At high k_θ, an interesting cascade of Alfvénic drift modes forms, starting at the ground state, with a simple parabolic-shaped $\delta\Phi$ eigenmode, and increasing to higher excited states with more nodes along the field lines as the plasma pressure gradient increases.

4. A set of newly-identified compressional electron drift modes is identified at high k_θ. These appear only when $\delta B_{\parallel}$ effects are included and are driven by simultaneous high beta and pressure gradient.

Finally, we note that analysis of this NSTX discharge has differed from previous experimental analysis of spherical torus plasmas, which have shown strongly unstable ETG modes [30] and micro-tearing modes [18, 19, 31]. In this analysis, we found the ETG modes to

be stable and no micro-tearing instabilities were observed. The former was found to be due mostly to the low temperature gradient, which is perhaps also for the same reason for the latter as the electron temperature gradient is believed to be a driver for these instabilities. Nevertheless, due to the high beta and strong pressure gradient effects, the same considerations apply. While in these studies our purpose was to elucidate beta and plasma pressure gradient effects, the importance of collisions, rotation, and impurities, particularly for NSTX which tends to have a large impurity concentration, also need to be considered for accurate experimental modeling. Including these effects and the necessary higher-resolution may make modeling the nonlinear gyrokinetic transport computationally challenging.

Acknowledgments

The authors would like to thank P.B. Snyder and R.E. Waltz for helpful discussions, and are thankful to S.M. Kaye for providing TRANSP analysis of the NSTX data and to the NSTX Team for carrying out the experiments that led to this data.

This research was supported by the U.S. Department of Energy under Grant DE-FG02-95ER54309 and by the Edge Simulation Laboratory project under Grant DE-FC02-06ER54873.

APPENDIX A

The spatial discretization of the differential operators required for construction of the Maxwell field matrix follows precisely the same approach as for the GYRO initial-value solver, with the various stencils and quadrature methods discussed in detail in Ref. [5]. The velocity-space variables in GYRO are

$$\lambda \doteq \frac{B_{\rm unit} v_\perp^2}{B v^2} \quad \text{and} \quad \varepsilon \doteq \frac{m_a v^2}{2T_a} \tag{A1}$$

Fluctuating quantities are evaluated on a species-independent mesh with radial nodes $\{r_i\}_{i=1}^{n_r}$, pitch-angle nodes $\{\lambda_k\}_{k=1}^{n_\lambda}$, energy nodes $\{\varepsilon_\mu\}_{\mu=1}^{n_\varepsilon}$ and orbit-time nodes $\{\tau_m\}_{m=1}^{n_\tau}$. The gyroaverage of the effective potential $\widetilde{\Psi}_a$, for species a, has the discrete representation

$$(\widetilde{\Psi}_a)_{ikm}^{\mu} = \sum_{i'\sigma} G_{ii'km}^{\sigma a \mu} \Phi_{i'km}^{\sigma} \ , \tag{A2}$$

where the three-potential Φ^σ at the same point in configuration space is given by the complex Galerkin representation

$$\Phi^\sigma_{ikm} = \sum_j c^\sigma_{ij} F_{ij}(\theta_{km}) \ . \tag{A3}$$

Here, c^σ_{ij} are the so-called *blending coefficients*, and F_{ij} the basis functions defined in Sections 5.2 and 5.3 of Ref. [5]. The propagator has the matrix form

$$P^{a\mu}_{ii'kk'mm'} = \omega\delta_{ii'kk'mm'} + (\omega_\theta)^{a\mu}_{ikmm'}\delta_{ii'kk'} + (\omega_d)^{a\mu}_{ii'km}\delta_{mm'kk'} + (\omega_C)^{a\mu}_{ikk'mm'}\delta_{ii'} \ . \tag{A4}$$

We can write the nonadiabatic distribution $\widetilde{H}_a$ in terms of the inverse of the propagator as

$$\left(\frac{\widetilde{H}_a}{f_{Ma}}\right)^{a\mu}_{ikm} = \frac{z_a e n_a}{T_a}(P^{-1})^{a\mu}_{ii'kk'mm'}(\omega - \omega^{a\mu}_{*i'k'm'}) \sum_\sigma G^{\sigma a\mu}_{i'i''k'm'} \sum_j c^\sigma_{i''j} F_{i''j}(\theta_{k'm'}) \ . \tag{A5}$$

Constructing the Galerkin projections of all three Maxwell equations, using the technique described in Section 5.3 of Ref. [5], yields the matrix equation

$$M^{\sigma\sigma'}_{ii'jj'}c^{\sigma'}_{i'j'} = \left[A^\sigma_{ii'jj'}\delta_{\sigma\sigma'} - B^{\sigma\sigma'}_{ii'jj'}(\omega)\right] c^{\sigma'}_{i'j'} = 0 \ , \tag{A6}$$

where

$$A^\sigma_{ii'jj'} = \sum_{km} F^*_{ijkm} L^\sigma_{ii'km} F^*_{i'j'km} \tag{A7}$$

and

$$B^{\sigma\sigma'}_{ii'jj'}(\omega) = \sum_{a\mu}\sum_{i'''km}\sum_{i''k'm'} \frac{z_a^2 e^2 n_a}{T_a} w^\mu_{km} F^*_{ijkm} G^{\sigma a\mu}_{ii'''km} (P^{-1})^{a\mu}_{i'''i''kk'mm'} (\omega - \omega^{a\mu}_{*i''k'm'}) G^{\sigma' a\mu}_{i''i'k'm'} F_{i'j'k'm'} \tag{A8}$$

$$= \sum_{a\mu}\sum_{p,p'} U^{a\mu}_{qp} (P^{-1})^{a\mu}_{pp'} V^{a\mu}_{p'q'} \tag{A9}$$

$$= B^{\sigma\sigma'}_{qq'} \ . \tag{A10}$$

Here, the weights w^μ_{km} are the products of the energy, pitch-angle and orbit-time weights defined in Eq. (72) of Ref. [5]. In terms of these weights, the flux-surface average of the velocity-space integration is written as

$$\mathcal{F}\int d^3v f_{Ma}\Psi_a \to \sum_{km\mu} w^\mu_{km}(\Psi_a)^\mu_{ikm} \quad \text{with} \quad \sum_{km\mu} w^\mu_{km} = 1 \ . \tag{A11}$$

In addition, we have defined the lumped indices $p = (i''', k, m)$, $p' = (i'', k'm')$, $q = (i, j, \sigma)$ and $q' = (i', j', \sigma')$. High performance is achieved by computing the inverse P^{-1} using

the LAPACK routines `ZGETRF` (LU decomposition) followed by `ZGETRI` (inverse), with the subsequent matrix triple-product $UP^{-1}V$ evaluated using two sequential calls to the BLAS `ZGEMM` kernel. Finally, $\det(M)$ is computed by the formula

$$\det(M) = \pm \prod_q L_{qq} \tag{A12}$$

where L is the lower-triangular matrix returned by the `ZGETRF` factorization. The upper (lower) sign is taken if an even (odd) number of row permutations were made in the factorization.

[1] T. Antonsen and B. Lane. *Phys. Fluids* **23**, 1205 (1980).

[2] E.A. Frieman and L. Chen. *Phys. Fluids* **25**, 502 (1982).

[3] H. Sugama and W. Horton. *Phys. Plasmas* **5**, 2560 (1998).

[4] M. Ono, S.M. Kaye, Y.-K.M. Peng, G. Barnes, W. Blanchard, M.D. Carter, J. Chrzanowski, L. Dudek, R. Ewig, D. Gates, R.E. Hatcher, T. Jarboe, S.C. Jardin, D. Johnson, R. Kaita, M. Kalish, C.E. Kessel, H.W. Kugel, R. Maingi, R. Majeski, J. Manickam, B. McCormack, J. Menard, D. Mueller, B.A. Nelson, B.E. Nelson, C. Neumeyer, G. Oliaro, F. Paoletti, R. Parsells, E. Perry, N. Pomphrey, S. Ramakrishnan, R. Raman, G. Rewoldt, J. Robinson, A.L. Roquemore, P. Ryan, S. Sabbagh, D. Swain, E.J. Synakowski, M. Viola, M. Williams, J.R. Wilson, and NSTX Team. *Nucl. Fusion* **40**, 557 (2000).

[5] J. Candy and R.E. Waltz. *J. Comput. Phys.* **186**, 545 (2003).

[6] M. Kammerer, F. Merz, and F. Jenko. *Phys. Plasmas* **15**, 052102 (2008).

[7] E.M. Bass. *Bull. Am. Phys. Soc.* **54**, 344 (2009).

[8] G. Rewoldt, W.M. Tang, and M.S. Chance. *Phys. Fluids* **25**, 480 (1982).

[9] G.L. Falchetto, J. Vaclavik, and L. Villard. *Phys. Plasmas* **10**, 1424 (2003).

[10] H. Sugama. *Phys. Plasmas* **6**, 3527 (1999).

[11] M. Kotschenreuther, G. Rewoldt, and W.M. Tang. *Comput. Phys. Commun.* **88**, 128 (1995).

[12] W. Dorland, F. Jenko, M. Kotschenreuther, and B.N. Rogers. *Phys. Rev. Lett.* **85**, 5579 (2000).

[13] M. Kotschenreuther, W. Dorland, Q.P. Liu, and M.C. Zarnstorff. *Nucl. Fusion* **40**, 677 (2000).

[14] M.N. Rosenbluth and M.L. Sloan. *Phys. Fluids* **14**, 1725 (1971).

[15] C.Z. Cheng and N.N. Gorelenkov. *Phys. Plasmas* **11**, 4784 (2004).

[16] C. Bourdelle, W. Dorland, X. Garbet, G.W. Hammett, M. Kotschenreuther, G. Rewoldt, and E.J. Synakowski. *Phys. Plasmas* **10**, 2881 (2003).

[17] A. Sykes, R.J. Akers, L.C. Appel, E.R. Arends, P.G. Carolan, N.J. Conway, G.F. Counsell, G. Cunningham, A. Dnestrovskij, Yu.N. Dnestrovskij, A.R. Field, S.J. Fielding, M.P. Gryaznevich, S. Korsholm, E. Laird, R. Martin, M.P.S. Nightingale, C.M. Roach, M.R. Tournianski, M.J. Walsh, C.D. Warrick, H.R. Wilson, S. You, MAST Team, and NBI Team. *Nucl. Fusion* **41**, 1423 (2001).

[18] C.M. Roach, D.J. Applegate, J.W. Connor, S.C. Cowley, W.D. Dorland, R.J. Hastie, N. Joiner, S. Saarelma, A.A. Schekochihin, R.J. Akers, C. Brickley, A.R. Field, M. Valovic, and the MAST Team. *Plasma Phys. Control. Fusion* **47**, B323 (2005).

[19] D.J. Applegate, C.M. Roach, J.W. Connor, S.C. Cowley, W. Dorland, R.J.Hastie, and N. Joiner. *Plasma Phys. Control. Fusion* **49**, 1113 (2007).

[20] J. Candy. *Plasma Phys. Control. Fusion* **51**, 105009 (2009).

[21] M.D. Kruskal and R.M. Kulsrud. *Phys. Fluids* **1**, 265 (1958).

[22] R.E. Waltz and R.L. Miller. *Phys. Plasmas* **6**, 4265 (1999).

[23] R.L. Miller, M.S. Chu, J.M. Greene, Y.R. Lin-liu, and R.E. Waltz. *Phys. Plasmas* **5**, 973 (1998).

[24] A. Zayed. *Handbook of Function and Generalized Function Transformations.* CRC Press, Boca Raton, (1996).

[25] A.M. Dimits, G. Bateman, M.A. Beer, B.I. Cohen, W. Dorland, G.W. Hammett, C. Kim, J.E. Kinsey, M. Kotschenreuther, A.H. Kritz, L.L. Lao, J. Mandrekas, W.M. Nevins, S.E. Parker, A.J. Redd, D.E. Shumaker, R. Sydora, and J. Weiland. *Phys. Plasmas* **7**, 969 (2000).

[26] M.J. Pueschel, M. Kammerer, and F. Jenko. *Phys. Plasmas* **15**, 102310 (2008).

[27] P.B. Snyder and G.W. Hammett. *Phys. Plasmas* **8**, 744 (2001).

[28] J. Candy and R.E. Waltz. *Phys. Rev. Lett.* **91**, 045001 (2003).

[29] N. Joiner, A. Hirose, and W. Dorland. *Phys. Plasmas* **17**, 072104 (2010).

[30] C.M. Roach, I.G. Abel, R.J. Akers, W. Arter, M. Barnes, Y. Camenen, F.J. Casson, G. Colyer, J.W. Connor, S.C. Cowley, D. Dickinson, W. Dorland, A.R. Field, W. Guttenfelder, G.W. Hammett, R.J. Hastie, E. Highcock, N.F. Loureiro, A.G. Peeters, M. Reshko, S. Saarelma, A.A. Schekochihin, and H.R. Wilson. *Plasma Phys. Control. Fusion* **51**, 124020 (2009).

[31] D.J. Applegate, C.M. Roach, S.C. Cowley, W.D. Dorland, N. Joiner, R.J. Akers, N.J. Conway, A.R. Field, A patel, M. Valovic, and M.J. Walsh. *Phys. Plasmas* **11**, 5085 (2004).